

Orbital Angular Momentum Multiplexing in Space–Time Thermoacoustic Metasurfaces

Yurou Jia, Yimin Liu, Bolun Hu, Wei Xiong, Yechao Bai, Ying Cheng,* Dajian Wu, Xiaojun Liu,* and Johan Christensen*

Multiplexing technology with increased information capacity plays a crucial role in the realm of acoustic communication. Different quantities of sound waves, including time, frequency, amplitude, phase, and orbital angular momentum (OAM), have been independently introduced as the physical multiplexing approach to allow for enhanced communication densities. An acoustic metasurface is decorated with carbon nanotube patches, which when electrically pumped and set to rotate, functions as a hybrid mode-frequency-division multiplexer with synthetic dimensions. Based on this spatiotemporal modulation, a superposition of vortex beams with orthogonal OAMs and symmetric harmonics are both numerically and experimentally demonstrated. Also, flexible combinations of OAM modes with diverse frequency shifts are obtained by transforming the azimuthal phase distributions, which inspires a mode-frequency-division multiplexing approach that significantly promotes the communication capacity.

dramatically boost the capacity and meet an unprecedented growth in data transmission, orbital angular momenta (OAM) carried by an artificial acoustic vortex constitutes an extra degree-of-freedom using mode-division multiplexing.^[6–9] At the same time, we witnessed rapid developments in generation, transmission and detection of optical vortex beams, which has provided a landscape of strategies for OAM multiplexing that are crucial to the practical applications of high-capacity optical communications.^[10–14] The OAM mode characterized by the topological charge l , describes the azimuthal eigenmodes of vortex beams with a phase singularity that are theoretically unbound in free space.^[15–17] The pioneering design to experimentally implement OAM modes into acoustic communications is based

1. Introduction

Multiplexing technology provides a promising solution to facilitate substantial increase of transmission capacity in acoustic communications.^[1,2] So far, basic physical quantities of sound waves such as time, frequency, amplitude, and phase have been widely utilized in multiplexing schemes, exhibiting considerable abilities in the extension of information channels and data content.^[3–5] Beyond those well-known variables, to

on transducer arrays, which are digitally controlled to generate multiplexed OAMs and the data information contained in each channel is extracted by using mode orthogonality relation.^[7] Using this scheme, a high spectral efficiency of $8.0 \pm 0.4 \text{ bits}^{-1} \text{ Hz}^{-1}$ has been obtained based on multiplexing eight different vortex beams. Acoustic metasurfaces are also constructed to enable fast OAM multiplexing and demultiplexing techniques by exploiting Helmholtz resonators to convert higher-order OAM modes into lower-order ones,^[6]

Y. Jia, Y. Liu, B. Hu, W. Xiong, Y. Cheng, X. Liu
Department of Physics
MOE Key Laboratory of Modern Acoustics
Collaborative Innovation Center of Advanced Microstructures
Nanjing University
Nanjing 210093, China
E-mail: chengying@nju.edu.cn; liuxiaojun@nju.edu.cn

Y. Bai
School of Electronic Science and Engineering
Nanjing University
Nanjing 210023, China

Y. Cheng, X. Liu
State Key Laboratory of Acoustics
Institute of Acoustics
Chinese Academy of Sciences
Beijing 100190, China

D. Wu
Jiangsu Key Lab on Opto-Electronic Technology
School of Physics and Technology
Nanjing Normal University
Nanjing 210023, China

X. Liu
College of Aerospace Engineering
Chongqing University
Chongqing 400044, China

J. Christensen
Department of Physics
Universidad Carlos III de Madrid
Leganés, Madrid ES-28916, Spain
E-mail: johan.christensen@gmail.com

 The ORCID identification number(s) for the author(s) of this article can be found under <https://doi.org/10.1002/adma.202202026>.

DOI: 10.1002/adma.202202026

which warrants the data capacity of 228.70 bits⁻¹ from two OAM channels by multiplexing the first- and second-order vortex beams.

So far, existing multiplexing techniques merge signals through individual physical quantities, yet establishing new multiplexing methodologies remains challenging but could open doors to even richer communication capacities. Time-varying artificial structures have recently materialized as a new paradigm for light and sound engineering. Optical space–time modulated metamaterials, characterized with variational constitutive parameters in both spatial and temporal domains,^[18] are attracting growing attention and hold promising potentials to extend freedoms for light manipulations.^[19–21] The optical spatial field conversions in a spatiotemporal periodic modulated system were accompanied by correlated harmonic frequency shifts, which enabled extensive practical applications such as optical isolators,^[22] frequency converters,^[23] Doppler cloaks,^[24] and nonreciprocal antennas.^[25,26] Subsequently, substantial efforts were successively devoted to mapping the idea of space–time modulations from optics to acoustics.^[27–29] By introducing steady fluid flows, one-way transport of topological edge sound^[30] and acoustic nonreciprocal circulators in structured metagratings^[31] were realized. With spatiotemporal modulated boundary conditions in acoustic waveguides, dynamic topological pumping^[32] and nonreciprocal transport^[33] have also been experimentally observed. Moreover, merging coding metasurfaces with space–time modulations makes diverse scattering functionalities distribute at different harmonics.^[34] Conclusively, spatiotemporal metamaterials can simultaneously manipulate sound field distributions and harmonic frequency responses without resorting to nonlinearities, which promises exciting possibilities in space-frequency-division multiplexing.

In this work, we overcome the limitations of present multiplexing schemes by implementing a hybrid mode-frequency-division multiplexing technique in acoustics. By combining spatiotemporal modulations with OAM modes, the synthesized dimensionality introduces entirely new physics and design philosophies to multiplexing devices. Exempt from moving fluids or dynamic phase modulation through bulky and complex devices, we conceive a spatiotemporal metasurface (STM) that harnesses broadband thermoacoustic sound generation in electrically driven carbon nanotube (CNT) films in combination with dynamic rotation. The combination of electro-thermoacoustic sound generation together with the dynamic rotation of the STM, endows the configuration with coveted space–time modulation and ensures the continuous phase variations over time. Precisely, the STM design contributes to a superposition of vortex beams carrying opposite OAM modes at distinct carrier frequency harmonics, which are confirmed through both numerical simulation and experimental verification. On the basis of hybrid characteristics between OAM modes and harmonic frequencies, multi-path information is encoded into azimuthal phase profiles and afterward decoded from different OAM channels with corresponding frequency responses. This approach offers tremendous opportunities to actively multiplex and modulate the transport of vortex information, with the potential to stimulate new functionalities in acoustic communication devices.

2. Results and Discussion

2.1. Models and Theory

Figure 1a illustrates the schematic diagram of utilizing an STM to enable the realization of mode-frequency-division multiplexing. The space–time modulated phase profile $\Phi(\varphi, t)$ imparted to the STM is

$$\Phi(\varphi, t) = \phi(\varphi + 2\pi f_m t) \quad (1)$$

where ϕ is the phase profile that depends both on the azimuthal coordinate φ and time t , whereas f_m denotes the modulating frequency. It is established that space–time modulations can provide extra momentum for transitioning a fundamental mode f_0 into higher-order harmonics $f_n = f_0 + n f_m$ in the adiabatic regime ($f_m \ll f_0$).^[35,36] where the integer n is the harmonic order. As shown in Figure 1a, acoustic waves of frequency f_0 emit from the STM and evolve as two opposite vortex beams carrying OAM modes $l = \pm 1$, which correspond to both red- and blue-shifted frequencies, that is, $f_0 - f_m$ and $f_0 + f_m$, respectively. To theoretically analyze such mode-frequency conversion phenomenon, we set the initially emitted acoustic wave to the following temporal form: $p(t) = p_0 e^{i2\pi f_0 t}$. Under spatiotemporal modulations of $\Phi(\varphi, t)$, the received acoustic waves are imprinted with linear phase shifts proportional to the phase term and harmonic order as^[37,38]

$$p_r(r, \varphi, z, t) = p_0 \sum_n a_n(r) e^{in\phi(\varphi)} e^{i2\pi(f_0 + n f_m)z/c_0} e^{i2\pi(f_0 + n f_m)t} \quad (2)$$

where r and z are the radial and axial coordinates, respectively, $a_n(r)$ describes the radial dependency of the n th harmonic field, $\phi(\varphi)$ represents the initial azimuth-dependent phase profile at $t = 0$, and c_0 is the speed of sound. In addition, the received acoustic waves exhibit azimuthal-dependence in the spatial domain, while their temporal responses can be expressed as a superposition of higher-order harmonics by using a Fourier decomposition

$$p_r(r, \varphi, z, t) = p_0 \sum_n b_n(r, \varphi) e^{i2\pi(f_0 + n f_m)z/c_0} e^{i2\pi(f_0 + n f_m)t} \quad (3)$$

where b_n is the expansion coefficient describing spatial dependence of the n th harmonic. Using the mutual orthogonality relationship between OAM modes of distinct orders, the spatially dependent coefficient b_n can be expanded as a sum over multiple OAM modes^[39]

$$b_n(r, \varphi) = \sum_l b_{n,l} c_l(r) e^{il\varphi} \quad (4)$$

with

$$b_{n,l} = \frac{\int_0^\infty \int_0^{2\pi} b_n(r, \varphi) b_l^*(r, \varphi) r dr d\varphi}{\int_0^\infty \int_0^{2\pi} b_l(r, \varphi) b_l^*(r, \varphi) r dr d\varphi} \quad (5)$$

where $b_l(r, \varphi) = c_l(r) e^{il\varphi}$ is a kind of vortex beam carrying l -order OAM with $c_l(r)$ being Bessel, Laguerre–Gauss or other modes, and the symbol $*$ denotes the complex conjugate of a variable.

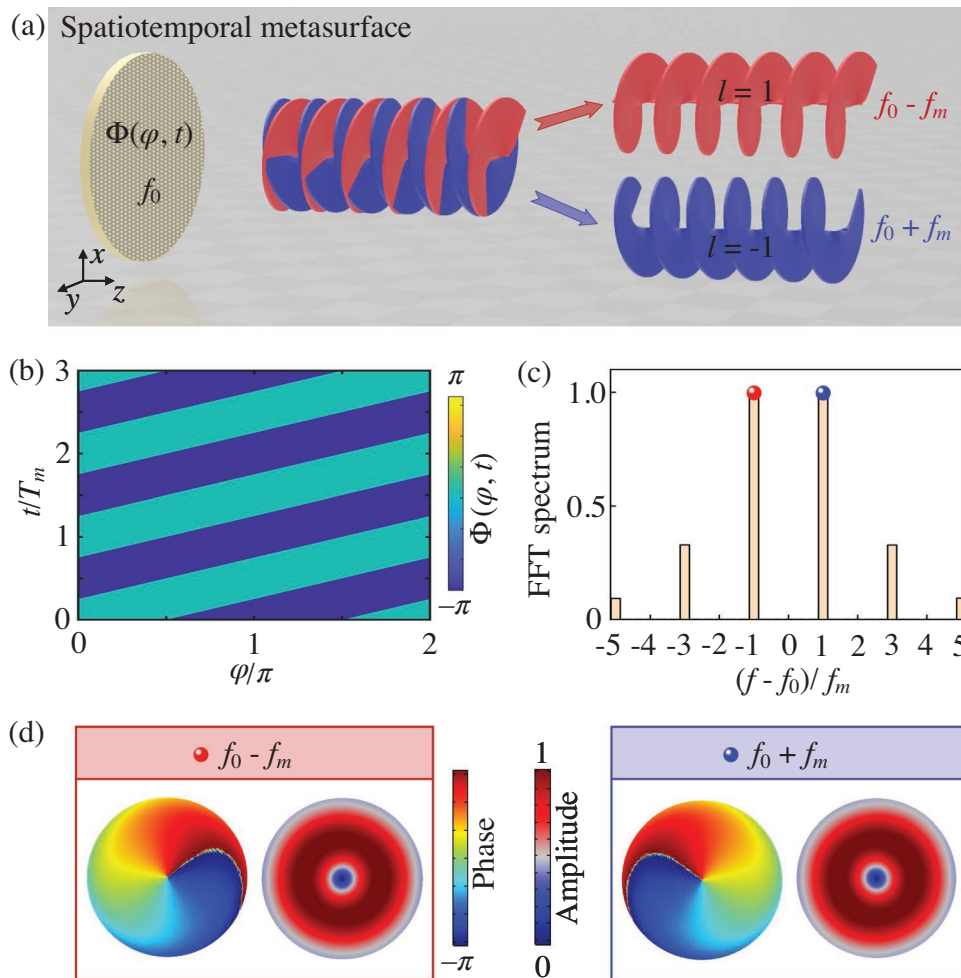


Figure 1. Spatiotemporal modulations for mode-frequency-division multiplexing. a) Schematic illustration of a spatiotemporal metasurface (STM) used to realize the acoustic mode-frequency-division multiplexing. b) Space–time phase modulation $\Phi(\varphi, t)$ imparted to the STM along the azimuthal direction φ with the modulation period T_m . c) Simulated output spectrum of the temporal sound fields after taking the fast Fourier transform (FFT). d) Simulated sound field distributions of the 1st-order (left panel) and –1st-order (right panel) vortex beams at the first-order harmonic frequencies of $f_0 - f_m$ and $f_0 + f_m$, respectively.

By substituting Equation (4) into Equation (3), the received acoustic waves are rewritten as

$$p_r(r, \varphi, z, t) = p_0 \sum_n \sum_l b_{n,l} c_l(r) e^{i\varphi} e^{i2\pi(f_0 + n f_m)z/c_0} e^{i2\pi(f_0 + n f_m)t} \quad (6)$$

Comparing Equation (6) with Equation (2), the received acoustic waves suggest a special relationship between the phase profile $\phi(\varphi)$, the harmonic order n , and the OAM state l through^[37]

$$n\phi(\varphi) = \arg \left[\sum_l b_{n,l} e^{i\varphi} \right] \quad (7)$$

where the operator **arg** is used to obtain the phase of a complex function. The ability to engineer the acoustic response of the STM, thus stems from the capacity to control $b_{n,l}$ (Equation (7)), which result in both spectrally and spatially diverse sound manipulation. In other words, the superposition states of OAMs with different topological charges and specific harmonic

responses can be flexibly adjusted by $b_{n,l}$ and the phase profile $\phi(\varphi)$, as shown schematically in Figure 1a.

Mode-frequency-division multiplexing requires space–time modulation of $\Phi(\varphi, t)$ ($T_m = 1/f_m$ is the modulation period) as shown in Figure 1b. For illustration, here the operating frequency f_0 is set to 6000 Hz, and the modulation frequency $f_m = 10$ Hz, which is far less than f_0 to satisfy the adiabatic condition. The phase profile $\phi(\varphi) = \arg[\cos(\varphi)]$ exhibits an azimuthal step function of units $-\pi$ and 0 , where the space–time modulated phase $\Phi(\varphi, t)$ dynamically changes along the azimuthal direction. Based on Equation (7), the dipole-like phase profile $\phi(\varphi) = \arg[\cos(\varphi)]$ can be presented as $\phi(\varphi) = \arg[e^{i\varphi} + e^{-i\varphi}]$ with the Fourier coefficient $b_{n,l} = 1$ at the first-order harmonics $n = \mp 1$, which guarantees two OAM modes $l = 1$ and -1 at the frequencies $f_0 - f_m$ and $f_0 + f_m$, respectively. To verify the generation of two opposite OAM modes with red- and blueshifted frequencies, the simulated output spectrum of the temporal sound fields after taking the fast Fourier transform (FFT) is shown in Figure 1c. We predict that most sound power resides at the

desired first-order harmonics $f_0 \pm f_m$, while less power levels distribute at the ensuing odd harmonics. The conversion efficiency from the fundamental frequency to first-order harmonics reaches about 65% (Note S1, Supporting Information). Further, in Figure 1d we present the simulated phase and amplitude profiles of the red- and blueshifted modes, that is, $f_0 \mp f_m$, as marked by red and blue dots in Figure 1c. The numerical simulations are performed based on the transient pressure acoustic module in COMSOL Multiphysics. A cylindrical domain is constructed with the radius of $0.875\lambda_0$ and height of $3\lambda_0$, where λ_0 is the acoustic operating wavelength at f_0 . The background medium is air with the mass density $\rho_0 = 1.21 \text{ kg m}^{-3}$ and sound speed $c_0 = 343 \text{ m s}^{-1}$. Cylindrical wave radiation conditions are imposed at the lateral boundaries to mimic free-space environment, and plane wave radiation conditions are imposed on the input and output boundaries to eliminate sound reflections. For ideal spatiotemporal modulations, the input boundary condition of the metasurface is set to the modulation phase $\Phi(\varphi, t) = \arg[\cos(\varphi + 2\pi f_m t)]$. The time dependent acoustic signals are calculated based on a transient solver with the time step of $0.1T_0$ ($T_0 = 1/f_0$), and the output spectra are obtained through a FFT solver. The cross-sectional observation plane locates at a distance $z = 0.5\lambda_0$ away from STM surface. In the left panel, the phase profile exhibits a center-singularity varying from $-\pi$ to π along the clockwise (CW) direction, while the amplitude profile with a center-null displays a concentric distribution; a known characteristic of a 1st-order vortex. On the contrary, in the right panel, the counterclockwise (CCW) varying phase profile and the ring-shaped amplitude distribution display the fingerprints of a -1st-order vortex beam.

2.2. Practical Design of STM

In order to implement the desired spatial phase modulation, we employ a rather flexible approach that relies on electrically pumping CNT film patches that are decorated on top of the metasurface. It has been previously reported that CNT films have superior characteristics comprising low heat capacitance and thermal inertia, which makes it a solid candidate to produce broadband and high intensity sound by means of electrothermoacoustic coupling.^[40–42] Here, a CNT film patch with the side lengths of 1 cm, thickness of $2 \mu\text{m}$ and the electrical resistance of 2.0Ω is shown in Figure 2a. When the CNT patch is pumped by an alternating voltage of 1.4 V, its thermograph displays an increased temperature of $28 \text{ }^\circ\text{C}$ compared to the ambient environment of $17 \text{ }^\circ\text{C}$. We place a microphone at 1 cm away from the CNT patch surface to detect the thermoacoustic generation of sound waves in response to the imposed periodic temperature oscillation as shown in Figure 2b. Its frequency of 6000 Hz is twice the frequency of the electrical pumping signal since the heat is generated during each half-cycle. In Figure 2c we further display the acoustic amplitude and phase shift as a function of the electrical signal delay. Our measurements show that the acoustic pressure amplitude remains uniform, while its phase accumulation doubles the electrical one. Hence, through appropriate manipulation of the electric phase delays, one is able to dynamically engineer the thermoacoustic phase generation as will. We fabricated a STM sample that consists

of three components as shown in Figure 2d. The uppermost layer comprises 42 pieces of CNT film patches that are pasted on a circular plate, which is made of high-performance heat-resistant nylon material through 3D-printing technology. The particular concentric CNT patch outline was chosen to ensure the best possible thermoacoustic coupling. Through suitably arranged electrical leads, the patches were connected to a printed circuit board disk, which was mounted on a holder that is of the same material as the circular plate. Lastly, the STM sample is mounted to an electric motor to generate the desired time-modulation. Unlike conventional loudspeaker arrays set to rotate, our CNT-film-based approach is virtually immune to centrifugal force at high-speed spatio-temporal modulations and resistant to the generation of unwanted turbulences.

2.3. Multiplexing Dual Vortex Beams

The entire experimental setup is seen in Figure 2e. To equip the STM sample with a spatial phase profile $\phi(\varphi) = \arg[\cos\varphi]$, we choose to segment the CNT film into smaller patches evenly arranged along the radial and azimuthal directions of STM (see Note S2, Supporting Information). Then, 42 square CNT patches with length of 10 mm are evenly divided into two parts with $\pi/2$ in electrical phase delay difference. As stated earlier, at an electric pump frequency of 3000 Hz, the stationary STM generates thermoacoustic sound at $f_0 = 6000 \text{ Hz}$ with an azimuthally step-wise varying phase, analogous to an acoustic dipole (Note S3, Supporting Information). However, when the electric motor sets to turn the STM at a constant CW rate of $f_m = 10 \text{ Hz}$, the measured (dots) FFT spectrum in Figure 2f reveals that the first-order harmonics at 5990 and 6010 Hz dominate the radiated sound fields, which is in good agreement with the simulated spectrum (histogram). Intuitively, a dipole can be considered as a superposition of two vortices carrying ± 1 OAM modes, thus the rotation of a dipole is equivalent to rotating both ± 1 st-order vortices. Based on the rotational Doppler effect,^[43] a 1st-order (-1st-order) OAM modes under the CW rotation rate of f_m can induce a frequency shift of $-f_m(f_m)$, which breaks the degeneracy between ± 1 st-order vortices and results in frequency-separated modes of distinct OAM modes.^[21] Note, in the simulation, instead of defining the incoming acoustic wave with the abovementioned space-time modulated phases, the cylindrical domain is split into a rotating one ($0.1\lambda_0$ in thickness) comprising the source and a static one ($2.9\lambda_0$ in thickness) used for wave propagation, in between which an identity boundary pair condition is imposed. The rotating domain that turns at the rate f_m contains 42 CNT square patches with a side length of 10 mm at the input, which are modeled as plane wave radiating surfaces with the time-independent phase shift $\phi(\varphi) = \arg[\cos\varphi]$, while the remaining region is considered sound hard. The static counterpart is set to be deformable with Laplace-type smoothing meshes. Lastly, continuity is imposed at the identity boundary pair between the rotating and deformable domains. We also emphasize the good agreement to the theoretical predictions discussed in Figure 1c, which should clearly corroborate our experimental approach to create spatiotemporal modulation. Note that a conventional phased array driven with spatial-temporal excitation can also realize the same effect, but

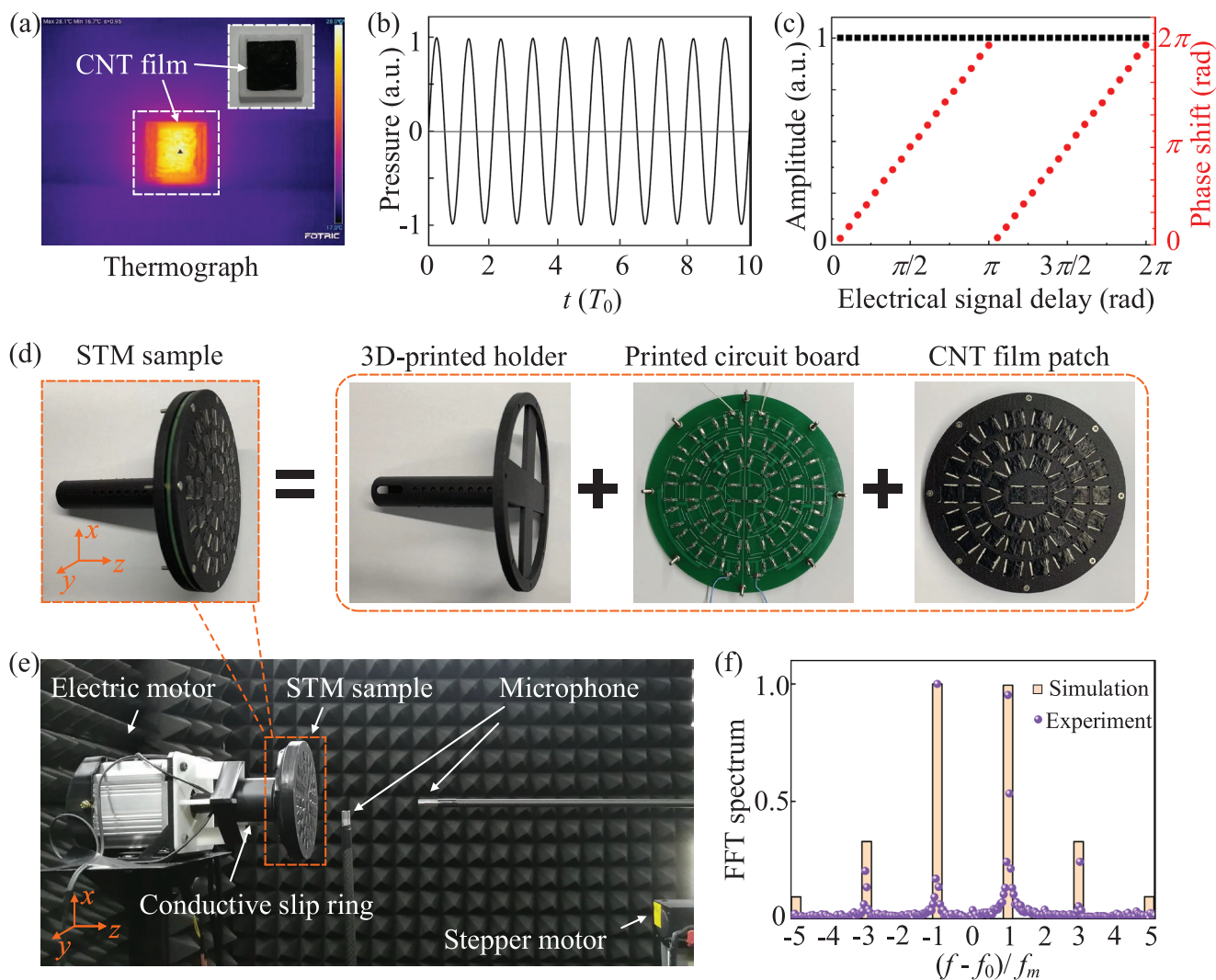


Figure 2. Practical design of the STM including the experimental setup for the sound field measurements. a–c) Electro-thermoacoustic response of a patch of electrically pumped CNT film. a) Photograph and thermograph of the sample. b) Temporal sound waveform received at 1 cm away from the CNT film patch. c) Amplitude (squares) and phase (dots) of sound signals with the variations of electrical signal delays. d) Fabricated STM prototype composed of three components: CNT film patches, printed circuit board disk, and 3D-printed holder. e) Photograph of the experimental setup for multiplexed sound field measurements. f) Measured (dots) and simulated (histogram) output FFT spectra from the STM sample with a constant rotation rate $f_m = 10$ Hz.

our rotational design is superior because it not only is exempt from complex dynamical electric control, but also creates a continuous phase translation along the time cycle.^[20]

The backbone of the hybrid mode-frequency division multiplexing is the splitting of the OAM modes into blue- and red-shifted components. The spatiotemporal modulation enables this, thus, we begin by studying the chirality of a dual vortex beam that carries these opposite OAMs. Hence, at a modulation rate of $f_m = 10$ Hz the spiraling fields of the first-order harmonic modes at frequencies 5990 and 6010 Hz are shown in **Figure 3a,d**, respectively. Considering unavoidable diffraction of sound waves in free space, both ± 1 st-order vortex beams extend to a distance about $1.5\lambda_0$, while their amplitude decreases (Note S4, Supporting Information). To enable the extended long-distance transmission of ± 1 st-order vortices, one can utilize a rigid cylindrical waveguide to localize sound energy with

minor dissipation (Note S5, Supporting Information). Their well agreeing simulated and measured cross-sectional phase and amplitude distributions of these ± 1 st-order vortex beams at distances $z = 0.5\lambda_0$ and $1.0\lambda_0$, are shown in **Figure 3b–f**. Small deviations of the amplitude profiles are mainly ascribed to fabrication errors of the experimental sample, while the slight discontinuities in phase profiles result from the measurement discretization along the orthogonal coordinates of the circular structure. We emphasize that such multiplexing scheme works efficiently, provided the adiabatic condition $f_m \ll f_0$ is met, for example, the ± 1 st-order vortex beams can be generated as well when $f_m = 20$ Hz, but their corresponding first-order harmonics reside at $f = 5980$ Hz and $f = 6020$ Hz (Note S6, Supporting Information). Moreover, mode-frequency-division multiplexing performs reliably as well at other spectral ranges from $f_0 = 3000$ Hz to 9000 Hz with an interval of 2000 Hz (Note S7,

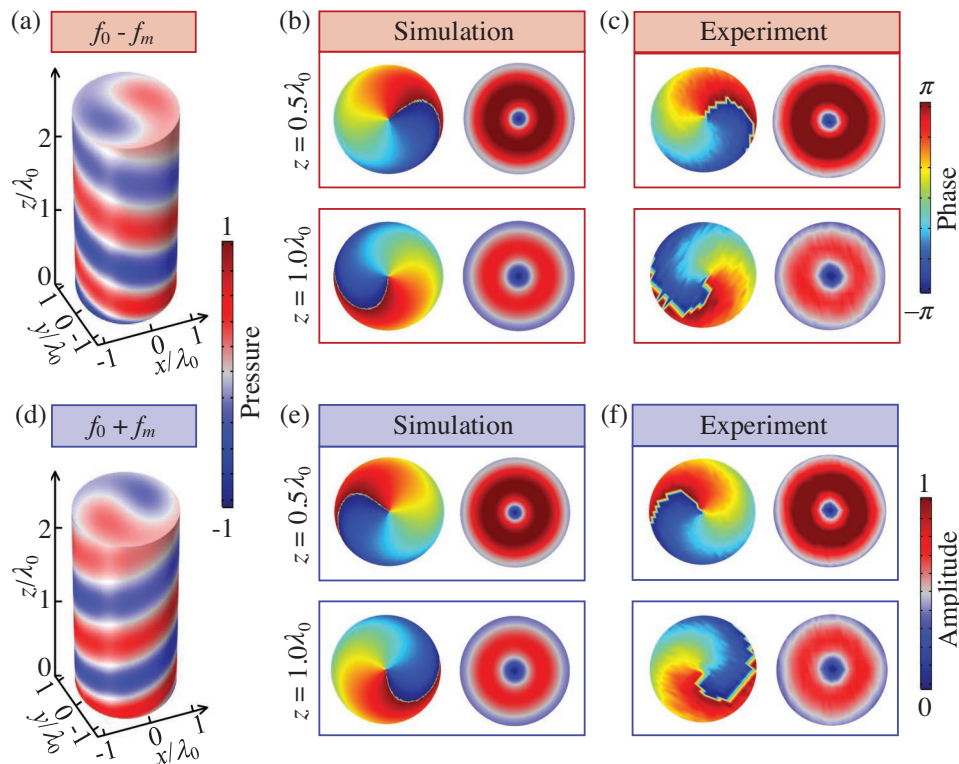


Figure 3. Experimental demonstration of dual vortex beams carrying opposite OAMs. a) Simulated sound field distribution of the first-order vortex beam at the first-order redshifted harmonic frequency of $f_0 - f_m$. b) Simulated and c) measured cross-sectional phase and amplitude distributions of the 1st-order acoustic vortex beams at the transverse planes $z = 0.5\lambda_0$ and $1.0\lambda_0$. d–f) Same as (a–c) but for the –1st-order vortex beam at the first blueshifted harmonic frequency of $f_0 + f_m$.

Supporting Information), thus the conservatively estimated relative bandwidth of the operation frequency range from 3000 to 9000 Hz already exceeds 100% (more than one octave), which can be regarded safely as a broadband response. We also conceive other binary phase profile $\phi(\varphi) = \arg[\cos(q\varphi)]$ at constant modulation rate f_m where the integer q describes the azimuthal periodic order (or the winding number), which leads to an additional symmetric spreading of the higher-order OAMs, that is, $f_0 \mp qf_m$ (Note S8, Supporting Information).

2.4. Spectrally and Spatially Diverse OAM Modes

The phase profile complexity plays a key role in the spectral and spatial richness of OAM modes. Unlike the binary phases profile discussed in the former, indeed we are able to engineer much more diverse phase textures. Hence, in **Figure 4a**, a more elaborate metasurface modulation of $\Phi(\varphi, t)$ is shown where the phase profile $\phi(\varphi) = \arg[e^{i\varphi} + e^{-2i\varphi}]$ continuously evolves at the modulating period of T_m . Maintaining the operating frequency $f_0 = 6000$ Hz and the modulating frequency $f_m = 10$ Hz for illustration, **Figure 4b** now displays how the sound power asymmetrically splits from the center operating frequency, in that most sound power resides at the first red (second blue)-shifted mode, that is, $f_0 - f_m$ ($f_0 + 2f_m$). Their respective phase and amplitude profiles clearly display the concurrent asymmetric harmonic OAMs of order $l = 1$ and $l = -2$ in **Figure 4c**.

Analogously, in **Figure 4d–f**, with a different phase profile $\phi(\varphi) = \arg[e^{i\varphi} + e^{3i\varphi}]$, this asymmetric spectrum gives rise to two redshifted vortices whose dominant OAM harmonics reside at $f_0 - f_m$ and $f_0 - 3f_m$. Moreover, when the phase profile is formed as $\phi(\varphi) = \arg[e^{-2i\varphi} + e^{3i\varphi}]$ in **Figure 4g**, an even broader splitting takes place in that the spectrum in **Figure 4h** is governed by a –3rd-order redshifted $f_0 - 3f_m$ and a 2nd-order blueshifted $f_0 + 2f_m$ mode, which respectively bring about orthogonal OAMs of order $l = 3$ and $l = -2$ as seen in **Figure 4i**. Note that the weights of these two vortices in the frequency spectra can be flexibly tuned through the amplitude modes in the phase profiles $\phi(\varphi)$ (Note S9, Supporting Information). We emphasize that in addition to the production of dual harmonic frequencies, so-called serrodyne frequency conversion can also be obtained using our approach. We numerically implement a phase profiles $\phi(\varphi) = \pm q\varphi$ that generates a single vortex beam with OAM modes $\pm q$ residing at the shifted frequencies $f_0 \mp qf_m$ (Note S10, Supporting Information). Interestingly, the serrodyne frequency conversion of OAM mode is subject to a rotational Doppler shift (Note S11, Supporting Information).^[43–45] Above all, using our space–time metasurface approach also enables the generation of fractional and extra high OAMs, whose shifted harmonic frequencies satisfy the relationship $f_0 \mp lf_m$ (Notes S12 and S13, Supporting Information). Generally speaking, we can summarize the present findings on diverse OAM conversions of the involved harmonics by their crucial importance in hybrid mode-frequency-division multiplexing.

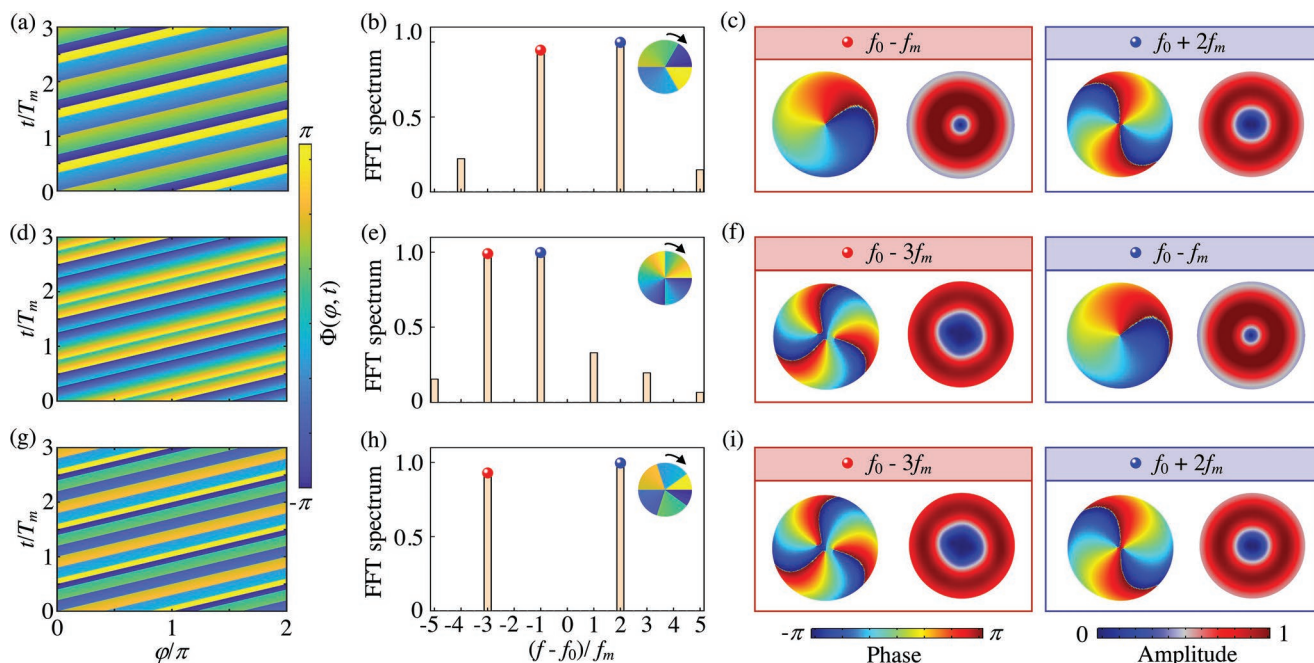


Figure 4. Spectral and spatial diversity of OAM modes. a) STM of $\Phi(\varphi, t)$ with the azimuthal phase profile $\phi(\varphi) = \arg[e^{i\varphi} + e^{-2i\varphi}]$. b) Corresponding output FFT spectrum. c) Cross-sectional phase and amplitude distributions of the vortex beams at two main harmonic frequencies marked by blue and red dots in (b). The corresponding results as in panels (a–c) but with the azimuthal phase profiles d–f) $\phi(\varphi) = \arg[e^{i\varphi} + e^{3i\varphi}]$ and g–i) $\phi(\varphi) = \arg[e^{-2i\varphi} + e^{3i\varphi}]$, respectively.

2.5. Communication using Mode-Frequency-Division Multiplexing

Finally, we take full advantage of the hybrid characteristics of the OAM modes and their tunable harmonics by implementing a multipath parallel communication system with unprecedented high capacity. In **Figure 5a**, three pictures of weather symbols “sunny,” “cloudy,” and “rainy” are discretized into $21 \times 21 = 441$ pixels, which are translated into three binary data streams in **Figure 5b**, denoted as H_1 , H_2 , and H_3 of “0” and “1” according to the “gray” and “black” colors in each pixel (e.g., “...0001000...,” “...0000010...,” and “...1110111...” correspond to the pixels labeled by the colored boxes in **Figure 5a**). In contrast to the current fundamental digital modulation techniques such as amplitude-, frequency-, or phase-shift keying, in **Figure 5c** three data streams H_1 , H_2 , H_3 are grouped and synchronously encoded onto the STM through the imprinted azimuthal phase profile $\phi_j(\varphi) = \arg[H_1 e^{i\varphi} + H_2 e^{-2i\varphi} + H_3 e^{3i\varphi}]$ (e.g., “... $\phi_1, \phi_1, \phi_1, \phi_4, \phi_1, \phi_3, \phi_1$...”), that is, a triple path parallel communication where j corresponds to the digital states “0,” “1,” ..., “7” derived from the 3-bit $H_1 H_2 H_3$ permutations such as “000,” “001,” ..., “111.” For real-time transfer, each group of multiplexed data is pulse modulated with one pulse cycle representing a burst period ranging from 0 to 0.3 s. For example, the phase profile ϕ_4 with $H_1 H_2 H_3 = 100$ transmits the data at cycle 11, and successively ϕ_1 with $H_1 H_2 H_3 = 001$ transmits at cycle 12. Thus, on the basis of this spatiotemporal modulation theory, the phase profiles ranging from ϕ_0 to ϕ_7 that are dynamically imposed on $\Phi(\varphi, t)$, accordingly generate different combinations of vortex beams carrying the OAM modes $l = 1$, $l = -2$, and $l = 3$ at their correlated frequency harmonics (Note S14, Supporting Information).

Subsequently, in **Figure 5d** a series of cycling phase profiles (... $\phi_1, \phi_1, \phi_1, \phi_4, \phi_1, \phi_3, \phi_1$...) are spatiotemporally modulated at the transmitted end, after which the three said data streams H_1 , H_2 , and H_3 are mapped on three independent vortex beams and their respective OAM modes $l = 1$, $l = -2$ and $l = 3$, which are marked by different colors. In the signal receiving process of the data stream contained in each OAM channel, on-off keying is employed where the presence or absence of vortex beams corresponds to the respective binary states “1” or “0.” Exempt from cumbersome sensors array and complex post-processing algorithms for OAM decoding,^[7] the “on” and “off” states of vortex beams can be spectrally retrieved on the basis of mode-frequency-division demultiplexing. Specifically, we determine the vortex beams by extracting the frequency responses at single point in the near-field (with coordinates $(0, 0.5\lambda_0, 0.5\lambda_0)$), that is, OAM modes $l = 1$, $l = -2$, and $l = 3$ respectively corresponding to the harmonic modes $f_0 - f_m$, $f_0 + 2f_m$, $f_0 - 3f_m$, instead of scanning the entire acoustic field. To further enable long-distance transmission of OAM information in the presence of diffraction, we can enlarge the radius of the metasurface for transferring spiral wavefronts from the near to the far field.^[8] In **Figure 5e**, the real-time received multiplexed signals within 441 cycles are demodulated into the temporal evolution of OAM harmonics by using the short-time Fourier transformations. For example, we only consider the data streams contained in the OAM channels $l = 1$, $l = -2$, and $l = 3$, which are decoded from the respective binary states of the vortex beams, and concurrently channeled as “...0001000...,” “...0000010...,” and “...1110111...” With the binary information “0” and “1” at each cycle represented by two different colors in each pixel, three distortion-free pictures are reconstructed from 441 cycles

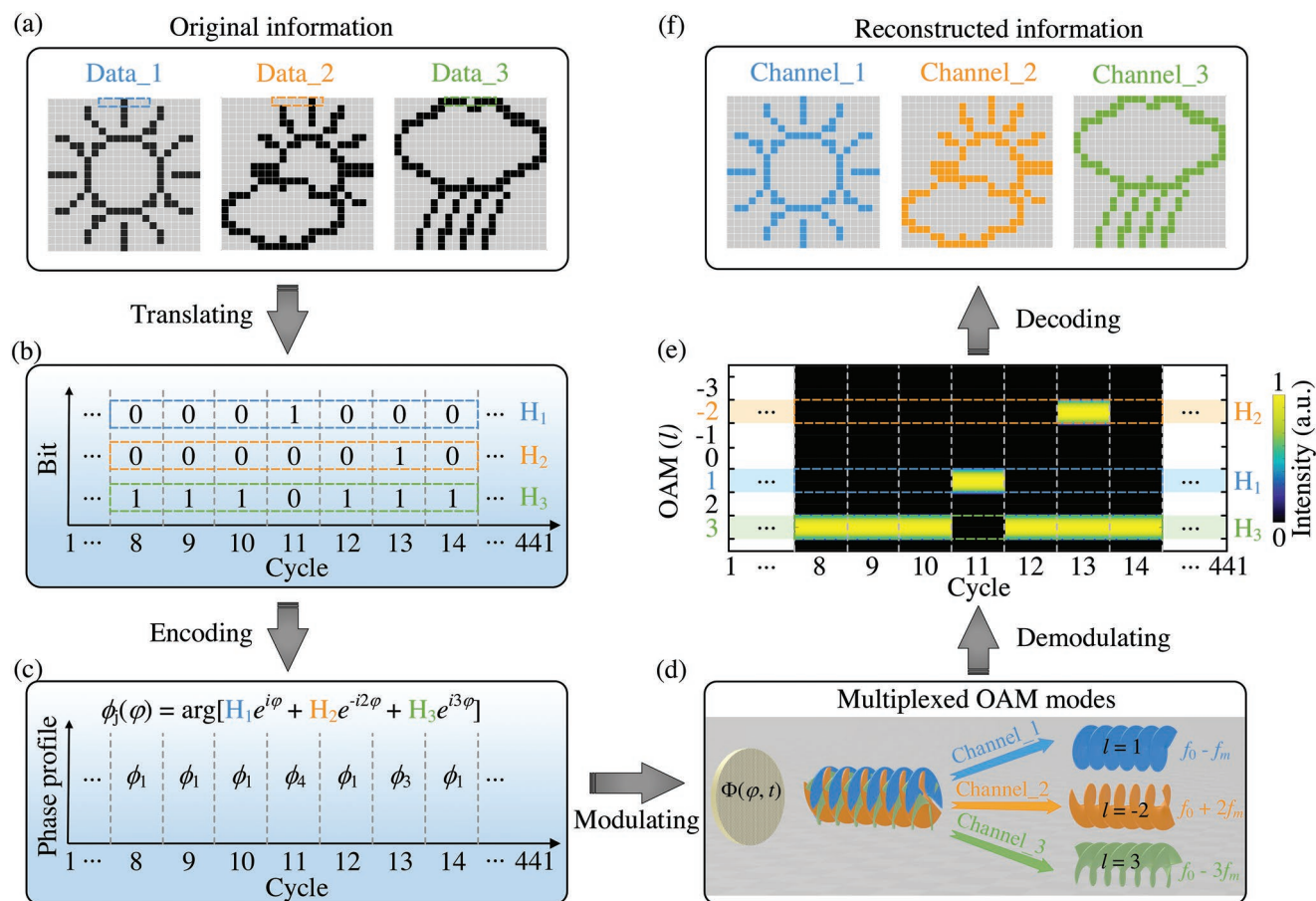


Figure 5. High-capacity parallel acoustic communication based on hybrid mode-frequency-division multiplexing. a) Three pictures of weather conditions: “sunny,” “cloudy,” and “rainy” discretized into 441 pixels. b) Their digital data translated into three binary data streams that are denoted as H_1 , H_2 , H_3 . c) Three data streams H_1 , H_2 , H_3 synchronously encoded onto the azimuthal phase profile $\phi_1(\varphi) = \arg[H_1e^{i\varphi} + H_2e^{-i2\varphi} + H_3e^{i3\varphi}]$. d) STM of $\Phi(\varphi, t)$ with $\phi_1(\varphi)$ used for triple-path parallel data transmission and the fast sound signal processing based on the mode-frequency-division demultiplexing. e) Demodulation of the real-time received multiplexed signals by using the short-time Fourier spectra. f) Reconstructed pictures from the recovered data streams in three demultiplexed vortex beam channels.

as “sunny,” “cloudy,” and “rainy” as shown in Figure 5f. The data capacity is 3.33 bits s^{-1} on each channel, therefore an aggregate capacity of 10 bits s^{-1} is obtained by multiplexing the three OAM channels ($l = 1$, $l = -2$, and $l = 3$). When the modulating frequency is set to $f_m = 0.1f_0$ (that is, 600 Hz) with the pulse period reduced to 0.005 s, an increased aggregate capacity of 600 bits s^{-1} can be obtained. Our approach shows that the flexible combination of OAM modes and frequency harmonics facilitates multi-path parallel signal transmission and fast data processing, which can significantly promote the development of high-capacity acoustic communication techniques. We emphasize also that in addition to multiplexing communications, the vortex modulation scheme is also constructed to realize high-base gray image transmission (Note S15, Supporting Information).

3. Conclusion

We have demonstrated a thermoacoustic approach to realize spatiotemporal modulation acoustic metasurfaces. By

patterning the metasurface with electrically pumped CNT patches, we were able to engineer the spatial phase profile at will. Moreover, by rotating the system using an electric motor, the additional time modulation was created. Compared with other spatiotemporal modulation schemes relying on complex phase arrays, our system leaps forward thanks to its compactness and reduced power consumption, which makes it appealing for a plethora of applications requiring a continuous and broadband spatiotemporal modulation. We theoretically, numerically and experimentally demonstrate that our approach enables us to access a diverse frequency spectrum of both symmetric and asymmetric OAM vortices, whose harmonic characteristics are a sole consequence of the reconfigurable imprinted spatiotemporal phase distribution. Moreover, we exploit the hybrid characteristics of the OAM modes and their frequency harmonics to realize yet unseen sound multiplexing. This procedure permits the encoding of multi-channel independent data streams into elaborate phase profiles, which are spatially multiplexed at the transmitter and afterward decoded from the OAM channels containing distinct frequency responses at the receiver.

Lastly, it is worth mentioning that dynamic switching between different OAM modes and frequencies in time not only enables high-capacity data transmission but also further increases the security of acoustic communication systems. For example, the hybrid mode-frequency division multiplexing technique enables fast recognition of different OAM modes and ensures the information security during the transmission process. Beyond that, its powerful capability of controlling the spectral distribution can be developed for frequency-hopping communications via joint multi-frequency modulation, which is promising to provide better performance in regards to confidentiality and anti-interference.^[46] Moreover, combining M OAM modes with N frequency modes facilitates $M \times N$ information channels, which substantially elevates the high capacity of data transmission in acoustic communication systems.^[47] Therefore, we envision that our methodology is a powerful tool that can potentially advance the application of vortex beams in acoustic communication techniques.

4. Experimental Section

The large area of CNT films of high uniformity was synthesized by high-temperature chemical-vapor-deposition method, which was further cut into 42 small square patches with the length of 1 cm by a laser cutting technology. The sheet resistance of each film measured as $2.0 \Omega \text{sq}^{-1}$ using a four-probe meter (type RTS-2, which complies with ASTM F84) fulfilled the experimental requirement of electrical properties. Then, the 42 CNT patches were pasted tightly on a circular plate with the diameter of 10 cm, which was made of heat-resistant nylon material through 3D-printed technology. Two edges of each CNT patch were fixed inside two shallow grooves of equal length in the circular plate and linked to the embedded conducting wires by silver paste. The assembled circular plate with CNT patches attached was connected with the printed circuit board (PCB) for the electrical signal supply. The CNT patches act not only as acoustic sources (emitters) but also as phase modulators, therefore, no external acoustic sources were needed in the experiments. A 3D-printed nylon holder finally mounted the circular plate and PCB with an electric motor.

The sound field measurements were carried out in an anechoic chamber to avoid the interferences of sound reflections. The excitation signals fed to the PCB were initially controlled by two clock-synchronized arbitrary waveform generators (NI PXIe-5423) through the preprogrammed LabVIEW software, and afterward amplified by the power amplifiers (YAMAHA P-5000). When the electric motor turned the STM sample at a constant rate for the desired time modulation, a conductive slip ring was used to ensure the stability of circuit connections between the PCB and the power amplifier during the rotation. In the measurement procedure, a 1/4-inch condensed microphones (GRAS40PH) was mounted on the stepper motor to scan the sound field distribution, while one additional microphone was fixed on a thin rod for phase reference. The output signals from the microphones were acquired by a digitizer (NI PXI-4499) and further processed using Matlab. In the experiments, accurate temperature control of CNT films was realized by an infrared thermal imager (FOTRIC 348) and a thermocouple thermometer (Fluke 52-II).

Supporting Information

Supporting Information is available from the Wiley Online Library or from the author.

Acknowledgements

This work was supported by National Basic Research Program of China (2017YFA0303702), NSFC (12074183, 11922407, 11834008, and 11874215), and the Fundamental Research Funds for the Central Universities (020414380181). J.C. acknowledges support from the European Research Council (ERC) through the Starting Grant 714577 PHONOMETEA.

Conflict of Interest

The authors declare no conflict of interest.

Data Availability Statement

The data that support the findings of this study are available from the corresponding author upon reasonable request.

Keywords

acoustic communication, mode-frequency-division multiplexing, multiplexing technology, spatiotemporal metasurface

Received: March 3, 2022

Revised: May 2, 2022

Published online: June 6, 2022

- [1] Y. F. Zhu, N. J. R. K. Gerard, X. X. Xia, G. C. Stevenson, L. Y. Cao, S. W. Fan, C. M. Spadaccini, Y. Jing, B. Assouar, *Adv. Funct. Mater.* **2021**, *31*, 2101947.
- [2] X. Jiang, C. Z. Shi, Y. Wang, J. Smalley, J. C. Cheng, X. Zhang, *Phys. Rev. Appl.* **2020**, *13*, 014014.
- [3] X. J. Shu, H. B. Wang, X. X. Yang, J. Wang, *Appl. Acoust.* **2016**, *105*, 200.
- [4] G. S. Zhang, H. F. Dong, *Ocean Eng.* **2011**, *38*, 1611.
- [5] C. B. He, Q. F. Zhang, Z. H. Yan, Q. Y. Li, L. L. Zhang, J. F. Chen, Q. Qi, *Ocean Eng.* **2017**, *145*, 207.
- [6] X. Jiang, B. Liang, J. C. Cheng, C. W. Qiu, *Adv. Mater.* **2018**, *30*, 1800257.
- [7] C. Z. Shi, M. Dubois, Y. Wang, X. Zhang, *Proc. Natl. Acad. Sci. USA* **2017**, *114*, 7250.
- [8] S. X. Gao, Y. B. Li, C. R. Ma, Y. Cheng, X. J. Liu, *Nat. Commun.* **2021**, *12*, 2006.
- [9] W. P. Li, M. Z. Ke, S. S. Peng, F. M. Liu, C. Y. Qiu, Z. Y. Liu, *Appl. Phys. Lett.* **2018**, *113*, 051902.
- [10] J. C. Ni, C. Huang, L. M. Zhou, M. Gu, Q. H. Song, Y. Kivshar, C. W. Qiu, *Science* **2021**, *374*, eabj0039.
- [11] D. Deng, H. Zhao, J. C. Ni, Y. Li, C. W. Qiu, *Nanophotonics* **2022**, *11*, 865.
- [12] J. C. Ni, S. L. Liu, D. Wu, Z. X. Lao, Z. Y. Wang, K. Huang, S. Y. Ji, J. W. Li, Z. X. Huang, Q. H. Xiong, Y. L. Hu, J. R. Chu, C. W. Qiu, *Proc. Natl. Acad. Sci. USA* **2021**, *118*, e2020055118.
- [13] Z. Jin, D. Janoschka, J. Deng, L. Ge, P. Dreher, B. Frank, G. Hu, J. Ni, Y. Yang, J. Li, C. Yu, D. Lei, G. Li, S. Xiao, S. Mei, H. Giessen, F. J. Meyer zu Heringdorf, C. W. Qiu, *eLight* **2021**, *1*, 5.
- [14] Y. J. Bao, J. C. Ni, C. W. Qiu, *Adv. Mater.* **2020**, *32*, 1905659.
- [15] B. Sanchez-Padilla, L. Jonusauskas, M. Malinauskas, R. Wunenburger, E. Brasselet, *Phys. Rev. Lett.* **2019**, *123*, 244301.
- [16] Y. Sebbag, U. Levy, *Opt. Lett.* **2020**, *45*, 6779.
- [17] P. Yu, J. X. Li, X. Li, G. Schutz, M. Hirscher, S. Zhang, N. Liu, *ACS Nano* **2019**, *13*, 7100.

- [18] M. K. Liu, D. A. Powell, Y. Zarate, I. V. Shadrivov, *Phys. Rev. X* **2018**, *8*, 031077.
- [19] A. M. Shaltout, V. M. Shalae, M. L. Brongersma, *Science* **2019**, *364*, 648.
- [20] L. Zhang, X. Q. Chen, S. Liu, Q. Zhang, J. Zhao, J. Y. Dai, G. D. Bai, X. Wan, Q. Cheng, G. Castaldi, V. Galdi, T. J. Cui, *Nat. Commun.* **2018**, *9*, 4334.
- [21] A. Mock, D. Sounas, A. Alù, *Phys. Rev. Lett.* **2018**, *121*, 103901.
- [22] N. Chamanara, S. Taravati, Z. L. Deck-Leger, C. Caloz, *Phys. Rev. B* **2017**, *96*, 155409.
- [23] X. C. Wang, A. Diaz-Rubio, H. N. Li, S. A. Tretyakov, A. Alù, *Phys. Rev. Appl.* **2020**, *13*, 044040.
- [24] L. Zhang, T. J. Cui, *Research* **2021**, *2021*, 9802673.
- [25] J. W. Zang, D. Correias-Serrano, J. T. S. Do, X. Liu, A. Alvarez-Melcon, J. S. Gomez-Diaz, *Phys. Rev. Appl.* **2019**, *11*, 054054.
- [26] L. Zhang, X. Q. Chen, R. W. Shao, J. Y. Dai, Q. Cheng, G. Castaldi, V. Galdi, T. J. Cui, *Adv. Mater.* **2019**, *31*, 1904069.
- [27] X. H. Wen, X. H. Zhu, H. W. Wu, J. S. Li, *Phys. Rev. B* **2021**, *104*, L060304.
- [28] R. Fleury, D. L. Sounas, C. F. Sieck, M. R. Haberman, A. Alù, *Science* **2014**, *343*, 516.
- [29] C. Shen, X. H. Zhu, J. F. Li, S. A. Cummer, *Phys. Rev. B* **2019**, *100*, 054302.
- [30] Y. J. Ding, Y. G. Peng, Y. F. Zhu, X. D. Fan, J. Yang, B. Liang, X. F. Zhu, X. G. Wan, J. C. Cheng, *Phys. Rev. Lett.* **2019**, *122*, 014302.
- [31] L. J. Fan, J. Mei, *Phys. Rev. Appl.* **2021**, *15*, 064002.
- [32] X. C. Xu, Q. Wu, H. Chen, H. Nassar, Y. Y. Chen, A. Norris, M. R. Haberman, G. L. Huang, *Phys. Rev. Lett.* **2020**, *125*, 253901.
- [33] W. T. Cheng, E. Prodan, C. Prodan, *Phys. Rev. Lett.* **2020**, *125*, 224301.
- [34] M. H. Fakheri, H. Rajabalipanah, A. Abdolali, *Phys. Rev. Appl.* **2021**, *16*, 024062.
- [35] M. M. Salary, S. Jafar-Zanjani, H. Mosallaei, *New J. Phys.* **2018**, *20*, 123023.
- [36] M. M. Salary, S. Farazi, H. Mosallaei, *Adv. Opt. Mater.* **2019**, *7*, 1900843.
- [37] H. B. Sedeh, M. M. Salary, H. Mosallaei, *Adv. Opt. Mater.* **2020**, *8*, 2000075.
- [38] H. B. Sedeh, M. M. Salary, H. Mosallaei, *Nanophotonics* **2020**, *9*, 2957.
- [39] Y. J. Yang, G. Thirunavukkarasu, M. Babiker, J. Yuan, *Phys. Rev. Lett.* **2017**, *119*, 094802.
- [40] L. Xiao, Z. Chen, C. Feng, L. Liu, Z. Q. Bai, Y. Wang, L. Qian, Y. Y. Zhang, Q. Q. Li, K. L. Jiang, S. S. Fan, *Nano Lett.* **2008**, *8*, 4539.
- [41] A. E. Aliev, N. K. Mayo, M. J. de Andrade, R. O. Robles, S. L. Fang, R. H. Baughman, M. Zhang, Y. S. Chen, J. A. Lee, S. J. Kim, *ACS Nano* **2015**, *9*, 4743.
- [42] B. L. Hu, Z. W. Zhang, H. X. Zhang, L. Y. Zheng, W. Xiong, Z. C. Yue, X. Y. Wang, J. Y. Xu, Y. Cheng, X. J. Liu, J. Christensen, *Nature* **2021**, *597*, 655.
- [43] G. M. Gibson, E. Toninelli, S. A. R. Horsley, G. C. Spalding, E. Hendry, D. B. Phillips, M. J. Padgett, *Proc. Natl. Acad. Sci. USA* **2018**, *115*, 3800.
- [44] M. Cromb, G. M. Gibson, E. Toninelli, M. J. Padgett, E. M. Wright, D. Faccio, *Nat. Phys.* **2020**, *16*, 1069.
- [45] H. L. Zhou, D. Z. Fu, J. J. Dong, P. Zhang, D. X. Chen, X. L. Cai, F. L. Li, X. L. Zhang, *Light Sci. Appl.* **2017**, *6*, e16251.
- [46] L. Zhang, M. Z. Chen, W. K. Tang, J. Y. Dai, L. Miao, X. Y. Zhou, S. Jin, Q. Cheng, T. J. Cui, *Nat. Electron.* **2021**, *4*, 218.
- [47] N. Bozinovic, Y. Yue, Y. X. Ren, M. Tur, P. Kristensen, H. Huang, A. E. Willner, S. Ramachandran, *Science* **2013**, *340*, 1545.